Enhanced performance stability of carbon/titania hybrid electrodes during capacitive deionization of oxygen saturated saline water

Pattarachai Srimuk[a,b], Marco Zeiger[a,b], Nicolas Jäckel[a,b,1], Aura Tolosa[a,b], Benjamin Krüner[a,b], Simon Fleischmann[b], Ingrid Grobelsek[a], Mesut Aslan[a], Boris Shvartsev[c], Matthew E. Suss[c,**], Volker Presser[a,b,*]

[a] INM—Leibniz Institute for New Materials, 66123 Saarbrücken, Germany
[b] Department of Materials Science and Engineering, Saarland University, 66123 Saarbrücken, Germany
[c] Faculty of Mechanical Engineering, Technion—Israel Institute of Technology, Haifa, 32000, Israel

A B S T R A C T

Capacitive deionization (CDI) is a promising technology for the desalination of brackish water due to its potentially high energy efficiency and its relatively low costs. One of the most challenging issues limiting current CDI cell performance is poor cycling stability. CDI can show highly reproducible salt adsorption capacities (SACs) for hundreds of cycles in oxygen-free electrolyte, but by contrast poor stability when oxygen is present due to a gradual oxidation of the carbon anode. This oxidation leads to increased concentration of oxygen-containing surface functional groups within the micropores of the carbon anode, increasing parasitic co-ion current and decreasing SAC. In this work, activated carbon (AC) was chemically modified with titania to achieve additional catalytic activity for oxygen-reduction reactions on the electrodes, preventing oxygen from participating in carbon oxidation. Using this approach, we show that the SAC can be increased and the cycling stability prolonged in electrochemically highly demanding oxygen-saturated saline media (5 mM NaCl). The electrochemical oxygen reduction reaction (ORR) occurring in our CDI cell was evaluated by the number of electron transfers during charging and discharging. It was found that, depending on the amount of titania, different ORR pathways take place. A loading of 15 mass% titania presents the best CDI performance and also demonstrates a favorable three-electron transfer ORR.

© 2016 Elsevier Ltd. All rights reserved.

1. Introduction

Developing energy efficient and cost effective techniques for the desalination of brackish and wastewater is a focal point of current research activities in environmental engineering [1–7]. Several techniques have been developed in the last decades, such as reverse osmosis, multistep distillation, electrodeionization and electrodialysis, and a particularly promising, fast-emerging method is capacitive deionization (CDI) [8–10]. Among electrochemical desalination methods, CDI has the particular advantages of operating at lower cell voltage and being based on a simple cell configuration. CDI is based on the reversible electrosorption of ions into an electrical double-layer within micropores of a saline water saturated porous carbon, typically activated carbon (AC). The fundamental principle of ion electrosorption can also be applied for energy storage in electrical double-layer capacitors (EDLCs) using electrolytes of high ionic strength. The adsorption capacity of the electrode material for CDI or the capacitance of EDLCs is dependent on the specific surface area of the carbon accessible to the ions [11,12]. Micro-mesoporous activated carbon is a widely used material due to specific surface areas (SSA) above $1000\,\mathrm{m^2\,g^{-1}}$.

During desalination by CDI, one electrode is negatively polarized and the second positively polarized. In a micropore, electric charge accumulates and is compensated in the electrolyte by co-ion expulsion or counter-ion adsorption (or a mixture of both processes) [13]. Co-ions denote ions with the same charge sign as the electrode charge, while counter-ions have a charge sign opposite to the electrode. Once the maximum possible number of

ions is electrosorbed by the porous electrode, the potential of the cell can be set to zero or reversed to release the ions and to regenerate the CDI electrodes. By this alternating operation, an effective purification of influent water is achieved and particularly high energy efficiencies have been obtained for saline media with low ionic strength [14]. It should be pointed out that only the adsorption of counter-ions contributes to the overall desalination. Co-ion expulsion consumes current without any contribution to the total desalination, resulting in reduced charge and energy efficiency, that is, the ratio between adsorbed salt over the accumulated charge [15]. To suppress the co-ion depletion and increase the overall charge efficiency, charge selective membranes can be used (membrane capacitive deionization, MCDI), or charged surface function groups can be added to the carbon micropores judiciously to enable enhanced or extended-voltage CDI [16–20]. Charge efficiency is a particularly informative CDI performance parameter, which gives the ratio of charge used for effective salt removal and total charge invested. The difference to 100% is mostly because of ion swapping and possible (parasitic) Faradaic side reactions which consume charge without contributing towards actual desalination; as a secondary effect, also contributions from resistive heating may have to be considered [21].

The concentration of surface groups, such as carboxyl groups, may increase especially in micropores *in-situ* during cycling of a CDI cell [22]. Such oxygen-containing surface groups are formed at the positively charged electrode due to carbon electro-oxidation in aqueous electrolytes, which is accelerated when dissolved oxygen is present. The result is a continuous performance decrease and low cell cycle life [23,24]. The effect of positively polarized electrode oxidation on the desalination performance of electrodes during CDI process is the focus of intensive research activities, and is currently the main limitation on CDI cell cycle life [22,25–27]. Current strategies to mitigate anode corrosion include nitrogen or argon purging of the feedwater [22], a reduction of cell potential as carbon oxidation takes place between 0.7 and 0.9 V vs. NHE [25], the use of chemical treatments to increase the concentration of negatively charged surface groups at the anode[28] (inverted-CDI), and the use of thin polymeric ion exchange membrane sheaths for the anode[29]. Yet, it is not always possible during practical applications to reduce the oxygen content by argon or nitrogen bubbling, and reducing cell voltage to avoid carbon oxidation comes at the cost of severely lowered desalination capacity. In inverted CDI (i-CDI), a high initial negative chemical charge concentration in the anode micropores led to the CDI process becoming fully inverted, whereby desalination occurred upon cell discharge [30–33]. While i-CDI allowed for mitigation of anode corrosion and long CDI cycle life of approximately 600 cycles, a key disadvantage of i-CDI at present is a rather low salt adsorption capacity (SAC). As shown by Gao et al., employing thin ion exchange membrane coatings directly on nanoporous carbon felt electrodes can significantly improve stability upon cycling[29] for desalination of de-aerated saline media. Membrane-free CDI, however, would be even more attractive due to the significant costs of ion exchange membranes [32]. Thus, there is an outstanding need for techniques to mitigate anode corrosion in a CDI cell without sacrificing SAC or other performance benchmarks.

Not only anode oxidation related to oxygen-containing functionalities needs to be addressed, but also the parasitic influence of dissolved oxygen on the CDI process [26,33,34]. Under realistic conditions, atmospheric oxygen (21 vol.%) diffuses into the water and electrochemically reacts with the carbon electrode during CDI operation. The widespread use of de-aerated saline solution in scientific literature does not correspond to the oxygen content in practical water applications.

The oxygen reduction reaction (ORR) either proceeds as a four or two-electron transfer, leading to hydrogen peroxide evolution as

the intermediate product, which can modify (and degenerate) the carbon surface [35]. The addition of metal oxides to the carbon electrode may contribute to overcoming the oxidation of the positively charged electrode and ORR, thus preventing performance fading and convey good aging stability of CDI. It has already been shown that a thin layer of metal oxide on the carbon material leads to better CDI performance [36–41]. Among several different metal oxides having ORR catalyst capability, such as MnO_2, Co_3O_4, Fe_2O_3, Fe_3O_4, and $NiCo_2O_4$ [42–47], titania appears to lead to significant improvement of ORR performance [48–50]. Particularly attractive is the high natural abundance and the facile nature of titania preparation methods, for example, by sol-gel processes [51–54]. The fundamental understanding of the mechanisms governing an improved salt adsorption capacity remains fragmented at present. Several factors play a role, including improved wettability, electrocatalysis, and enhanced charge separation due to possible negatively charged surface groups [55–59].

To the best of our knowledge, the influence of titania on the electro-oxidation, ORR, and aging stability of carbon-based CDI electrodes has not been investigated so far. For that task, we prepared hybrid electrodes consisting of activated carbon with different titania loadings, following a well-established sol-gel approach. The electrochemical properties, including oxygen reduction reaction (ORR), were systematically studied. CDI performance is tested in oxygen saturated aqueous NaCl, in particular with respect to aging stability, and the influence of titania loading on the performance is investigated. The key goal of our work is to establish the promising nature of carbon/metal oxide hybrid materials for enhanced CDI performance *stability* and to explore the underpinning electrochemical mechanisms enabling such performance.

2. Experimental

2.1. Synthesis of AC-titania hybrids

YP80-F activated carbon (AC) from Kuraray was used as electrode material. Ti(IV) isopropoxide was purchased from Sigma Aldrich. AC- titania hybrid materials were prepared by sol-gel method using one and two step hydrolysis reaction [40,41,60]. Different mass ratios of Ti(IV) isopropoxide to AC, dispersed in ethanol, were used to achieve different mass loadings of titania on AC.

Ti(IV) isopropoxide was first dissolved in 400 mL absolute ethanol. In all steps, the container was backfilled with argon. The amount of Ti(IV) isopropoxide (39.6, 46.6, 55.9, and 83.9 g) was calculated based on titania formation with regard to AC, which translates to 20, 25, 30, and 45 % of titania. In a second step, AC powder (30 g for each batch) was vacuum dried at 120 °C and 20 mbar for 10 h and put in an argon backfilled glass bottle, which was stirred for 5 h after adding of 400 mL ethanol. The resulting carbon slurry was subjected to ultrasound assisted bath (Sonorex Super RK514BH, Bandelin) for 30 min and afterwards poured into the Ti(IV) isopropoxide solution (55.9 and 83.9 g of Ti(VI) propoxide in 400 mL absolute ethanol) during stirring and kept stirred for 48 h. For the one step hydrolysis process, 39.6 and 46 g of Ti(IV) isopropoxide in 400 mL ethanol was centrifuged for solid/liquid separation and the removal of the unreacted excess isopropoxide. This was repeated for two times after re-dispersion of the sediment in 800 ml absolute ethanol. For the two step hydrolysis reaction, water was added to the AC-isopropoxide mixture in the first step and stirred for another 48 h to hydrolyze the amount of isopropoxide, which did not react with the AC surface. The molar ratio of water to isopropoxide was 5:1 for all batches. The settled material obtained after centrifugation was vacuum dried at 120 °C and 20 mbar for 10 h.

2.2. Structural and chemical characterization

Scanning electron microscope (SEM) images were recorded with a JEOL JSM 7500F field emission scanning electron microscope (FESEM, Japan) operating at 3 kV. Energy dispersive X-ray spectroscopy (EDX) was carried out in the system with an X-Max Silicon Detector from Oxford Instruments using AZtec software. Transmission electron micrographs were taken with a JEOL 2100F transmission electron microscope at 200 kV. Powder samples were prepared by dispersing them in ethanol and drop casting them on a copper grid with lacey carbon film (Gatan).

Raman spectra were measured with a Renishaw inVia Raman microscope using a Nd-YAG laser with an excitation wavelength of 532 nm. The system employed a grating with 2400 lines mm^{-1} yielding a spectral resolution of $\sim$1.2 cm^{-1} and the spot size on the sample was in the focal plane $\sim$2 μm with an output power of 0.2 mW. Spectra were recorded for 20 s and accumulated 10-times to obtain a high signal-to noise and signal-to-background ratio. Peak fitting was performed by employing four Lorentzian peaks for the spectrum between 900 cm^{-1} and 1900 cm^{-1}.

X-ray diffraction (XRD) was conducted employing a D8 Advance diffractometer (Bruker AXS) with a copper X-ray source ($Cu_{K\alpha}$, 40 kV, 40 mA) in point focus (0.5 mm) and a Goebel mirror. A VANTEC-500 (Bruker AXS) 2D detector ($\sim$25° per step; measurement time 1000 s per step) was employed. The samples were dispersed in ethanol and drop casted on a sapphire wafer to obtain a homogeneous layer. The sample holder was oscillating in plane (amplitude 5 mm with the speed of 0.5 mm s^{-1} along x and 0.2 mm s^{-1} along y) to enhance statistics.

Nitrogen gas sorption measurements at -196 °C were carried out with an Autosorb 6 B from Quantachrome. The powder samples were outgassed at 250 °C for 10 h under vacuum conditions at 10^2 Pa to remove adsorbed water; the outgassing temperature for film electrodes was 120 °C. Nitrogen gas sorption was performed in liquid nitrogen in the relative pressure range from 0.008 to 1.0. The BET-specific surface area (BET-SSA) was calculated with the ASiQwin-software using the Brunauer-Emmett-Teller[61] equation in the linear relative pressure range of 0.01-0.05. The DFT-specific surface area (DFT-SSA) and pore size distribution (PSD) were calculated via quenched-solid density functional theory (QSDFT)[62] with a model for slit pores.

Thermogravimetric analysis was carried out on dried hybrid samples at 10 °C min^{-1} to 900 °C in flowing synthetic air (10 cm^3 min^{-1}) to determine the ash content, which was used to calculate the total titania content in the samples (TG 209F1, Netzsch).

2.3. Electrochemical measurements

For electrochemical characterization, two types of electrodes were prepared: free-standing PTFE-bound electrodes for electrochemical characterization and drop casted film electrodes on graphite current collectors using PVP and PVB as binder for CDI [63,64]. Film electrodes were prepared by mixing AC powder or AC-titania hybrid powders with 5 to 10 mass % of dissolved polytetrafluoroethylene (PTFE, 60 mass% solution in water from Sigma Aldrich) and ethanol to obtain a homogeneous carbon paste. The carbon paste was rolled with a rolling machine (MTI HR01, MIT Corp.) to 180-200 μm thick, free standing film electrodes and dried in vacuum at 120 °C for 24 h at 20 mbar. The electrodes for CDI experiments were 6×6 cm^2 in size with a hole in the middle of each electrode of 1.5×1.5 cm^2, which was cut from the rolled film electrodes.

To evaluate the effect and electrochemical performance of titania in as prepared AC-titania hybrid materials, electrochemical analysis was carried out in three-electrode cells using Pt wire as a counter electrode, Ag/AgCl (3 M KCl, MF-2052 RE-5B, BASi Corp.) as

a reference electrode, and glassy carbon (3 mm diameter, MF-2012, BASi Corp) as substrate for a working electrode. Before use, the glassy carbon electrode was polished using aqueous alumina suspension on felt pad. The carbon hybrid slurry was prepared by dispersing 100 mg of as-prepared material and 2.5 mg of poly-vinylpyrrolidone (PVP) in 10 mL of ethanol. After tip sonication for 10 min, 5.85 mg of polyvinyl butyral (PVB; 25 mass% in ethanol) was added into the solution and stirred for 30 min. 5 μL of the resulting suspension was drop casted over glassy carbon electrode and dried at 60 °C for 30 min. The stability of the PVP/PVB binder for aqueous media was established in a previous publication[63] and confirmed by recent work by the group of Likun Pan [65].

Prior to the oxygen reduction reaction measurement, N_2 or O_2 gas was bubbled into aqueous 1 M NaCl for 20 min to achieve the de-aerated or O_2 saturated electrolytes, respectively. Cyclic voltammetry was used with a potential between -1.0 V to +0.6 V vs. Ag/AgCl with scan rates from 5 mV s^{-1} to 50 mV s^{-1}. The symmetric full-cell charge storage behavior of all samples was measured via cyclic voltammetry with a cell voltage from 0 to 1.2 V at scan rate of 5 mV s^{-1} and galvanostatic charge-discharge measurements with specific currents from 0.1 to 10 A g^{-1}. The as prepared free-standing electrodes were cut into 3×3 cm^2 pieces and placed between the graphite current collector (CC) of same size (SGL Technologies; thickness: 250 μm) and the porous separator (glass fiber pre-filter, Millipore, compressed thickness of a single layer is 380 μm) in the following order: CC/electrode/ spacer/electrode/CC. The stack was compressed and soaked in de-aerated 1 M NaCl. The specific capacitance of one electrode was calculated from galvanostatic cycling by applying different specific currents (0.1-10 A g^{-1}, normalized to both electrodes) and using Eq. (1):

$$C_{specific} = 4 \cdot \int_{t_1}^{t_2} I dt / U \cdot m \tag{1}$$

with I the measured current, t_2-t_1 the discharge time, U the applied cell voltage (with respect to iR drop), and m the mass of both electrodes.

2.4. CDI testing

A CDI setup described in Ref. [12] with flow-by electrodes was used to characterize the desalination performance. The CDI stack was built from graphite current collectors (SGL Technologies; thickness: 250 μm) with attached porous carbon film electrodes and a porous spacer (glass fiber pre-filter, Millipore, compressed thickness of a single layer is 380 μm). The measurements were carried out with three pairs of electrodes. So, each stack consisted of six electrodes, four CC and two parallel flow paths which were firmly pressed and sealed. The total masses of the CDI electrodes are 400, 844, 844, and 809 mg for AC, AC-15, AC-25, and AC-35, respectively. The total electrolyte flow rate was 22 mL min^{-1}. Ion adsorption and desorption steps were carried out using constant potential mode at 1.2 V. The electrode regeneration was accomplished at 0 V. For all electrochemical operations, we used a VSP300 potentiostat/galvanostat (Bio-Logic) and the duration of each half-cycle was 30 min. All experiments were carried out with 5 mM NaCl solution and a 10 L electrolyte tank which was flushed continuously with O_2 gas to obtain oxygen saturation in the electrolyte. The salt adsorption capacity and the measured charge were defined per mass of active material in both electrodes and were calculated as an average value from adsorption and desorption step. For quantification of the electrical charge, the leakage current measured at the end of each half-cycle was subtracted.

3. Results and discussion

3.1. Structural and chemical properties

The morphology of the electrode materials was studied with electron microscopy, see Fig. 1. The AC-15 sample reveals a smooth morphology compared to initial AC sample, indicating titania is coating the carbon surface homogeniously (Fig. 1C). As depicted in Fig. 1E, G, higher titania loadings lead to smoother surfaces, as also confirmed by TEM micrographs shown in Fig. 1D, F, H. Titania formation occurs when Ti(IV) isopropoxide is hydrolyzed at oxygen containing surface groups of AC even without the need for additional water (Fig. 1D) [40]. By a two-step hydrolysis, additional titania formation takes place on the initially formed titania layer, leading to continuous thickening of the coating (Fig. 1G, H).

The microstructure of the AC sample is clearly visible in the TEM image, with graphitic nanodomains connected by amorphous regions (Fig. 1B) [66]. After coating with titania, the AC structure is less visible due to the coverage with incompletely crystalline titania (AC-15, Fig. 1D). Once the titania mass loading is increased, nanocrystalline domains of titania occur across the surface for AC-25 and AC-35 (Fig. 1F, H). To examine the uniformity of titania coatings for all synthesis conditions, EDX mapping was conducted (Supplementary Information, Fig. S1), confirming a high uniformity of titanium and oxygen distribution.
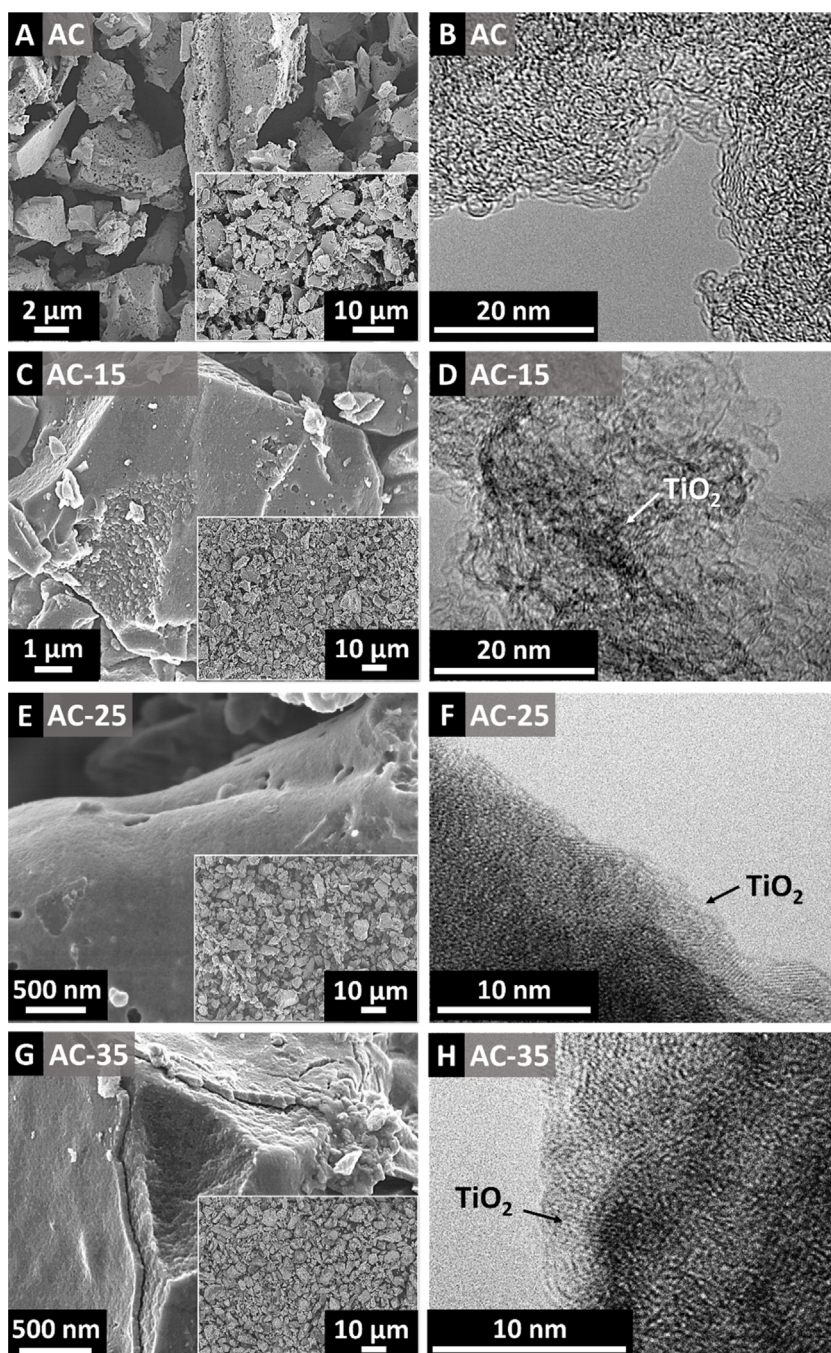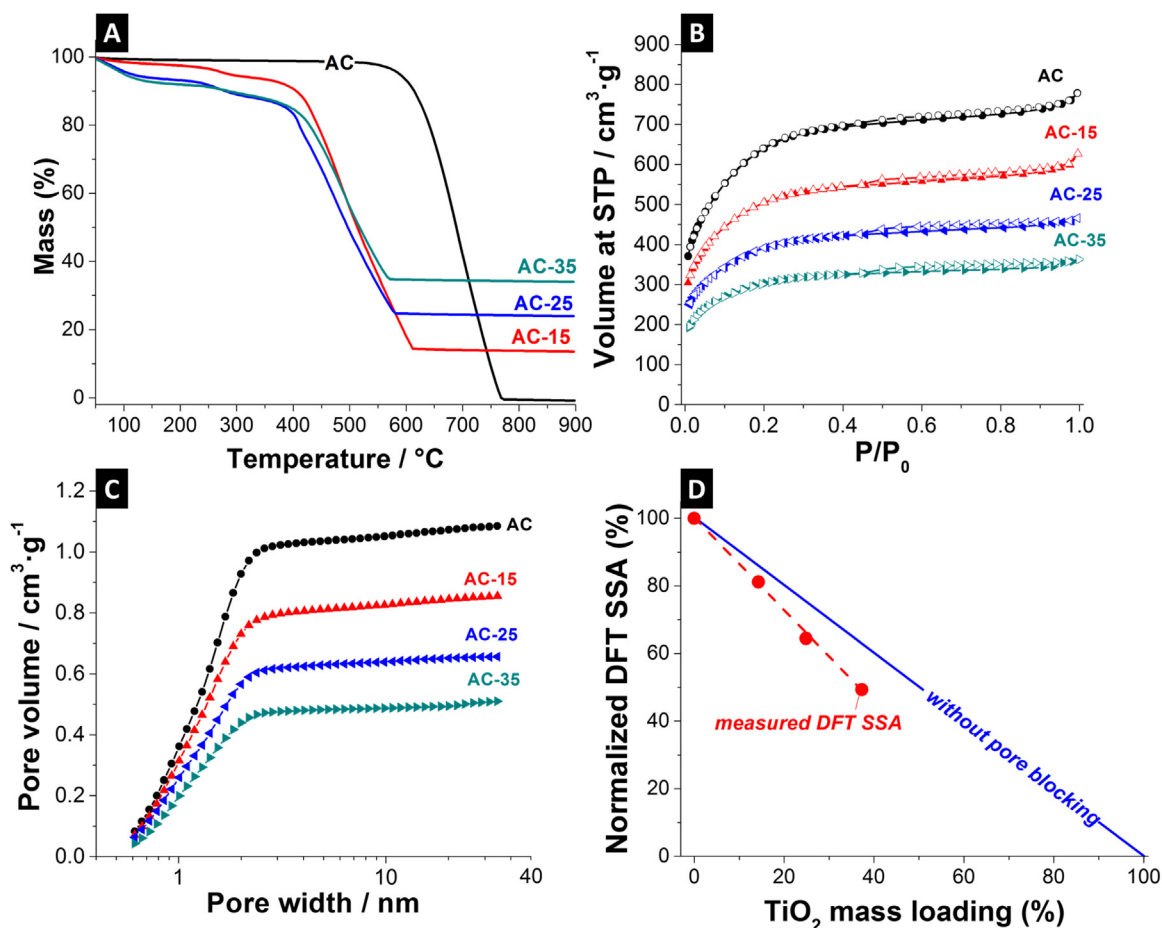

Fig. 1. Scanning electron micrographs (A,C,E,G) and transmission electron micrographs (B,D,F,H) of (A,B) AC, (C,D) AC-15, (E,F) AC-25, and (G,H) AC-35.

Fig. 2. (A) TGA curves, (B) nitrogen sorption isotherms at standard temperature and pressure (STP), (C) specific cumulative pore volumes, and (D) relative surface areas of AC, AC-15, AC-25, and AC-35.

The amount of titania in the AC/titania hybrids was quantified with TGA (Fig. 2A). AC is completely burned off between 600 °C and 800 °C, whereas AC-titania hybrids show a three-step mass loss. Between 50 °C and 150 °C, adsorbed water as well as unstable functional groups desorb from the surface alongside with a mass loss of 2.5-8.0 mass% [51]. Starting at 250 °C, loss of surface water and other volatile surface species accounts to ca. 5 mass% [67]. The carbon in the hybrid materials starts to burn off at 400 °C. This is a much lower temperature than the AC powder and can be explained by catalytic effects of the metal oxide [41,68]. At 600 °C, the carbon is completely removed and the titania coating remains (Table 1). It was found that the nominal (expected) titania contents of 20, 30, and 45 mass% lead to a mass loading in the hybrid material of titania mass of 14, 25, and 37 mass%, respectively (Table 1).

An increasing metal oxide loading is expected to partially block the AC nanopores and consequently decreases the specific surface area. The porosity and the surface area were analyzed using nitrogen sorption with the respective isotherms shown in Fig. 2B. All isotherms exhibit a characteristic type I(b) shape suggesting micropores with pores sizes smaller than 1.2 nm and 2.9 nm [69]. The specific surface area (DFT and BET) and the pore volumes are summarized in Table 2. As expected, the specific surface area (SSA) is decreased with increasing titania loading. Neat AC shows a BET-SSA of 2170 m² g⁻¹ (QSDFT-SSA = 1838 m² g⁻¹). When increasing the titania loading, the BET-SSA decreases to 1749 m² g⁻¹ (QSDFT-SSA = 1492 m² g⁻¹) for AC-15 and 1057 m² g⁻¹ (QSDFT-SSA = 907 m² g⁻¹) for AC-35. Due to the uniform titania covering of AC particles (Fig. 1G, H), pores are blocked when the titania content is increased (Fig. 2B, C). This is clearly seen in Fig. 2D, which shows the relative decrease of the surface area dependent on the metal oxide loading. An ideal dependency would correspond to titania addition without pore blocking; however, all hybrids fall below the ideal behavior, which indicates that pore blocking occurs for all samples to a certain degree. This pore blocking behavior is in line

Table 1
Results of TG analyses of AC-titania hybrids with different nominal titania contents, prepared by hydrolysis of AC Ti(IV) isopropoxide mixtures (heating rate 10 K min⁻¹, 900 °C, flowing air 10 cm³ min⁻¹).

Sample name	Nominal titania content (mass%)	Burn off residue (mass%)	Titania residue (mass%)
AC	0	0.5	–
AC-15	20	14.8	14.3
AC-25	30	26.4	24.9
AC-35	45	37.8	37.3

Table 2
Summary of the results of nitrogen GSA analyses at −196 °C of all AC-titania hybrids.

Sample name	SSA (m² g⁻¹)		Pore size (nm)	Pore volume (cm³ g⁻¹)
	BET	DFT	DFT	DFT
AC	2170	1838	1.30	1.09
AC-15	1749	1492	1.25	0.86
AC-25	1328	1185	1.20	0.66
AC-35	1057	907	1.20	0.51

with the findings of a recent study by our group investigating the hybridization of activated carbon with vanadia [70].

Structural and phase-dependent changes caused by the titania hybridization of AC were further assessed by Raman spectroscopy (Fig. 3). The Raman spectrum of the AC sample is typical for disordered and partially amorphous carbon materials [71]. It presents a D-mode at 1339 cm^{-1} and a G-mode at 1601 cm^{-1}, together with a significant fraction of amorphous carbon at ~1520 cm^{-1}. The detailed carbon structure of this commercial AC has been described in more detail in one of our previous works [69]. For AC and AC-titania hybrids, the same position of D- and G-band are measured with 1339 cm^{-1} for the D-mode and 1601 cm^{-1} for the G-mode. Peak deconvolution revealed small changes of the areal intensity ratio I_D/I_G, with 2.0 for AC, 2.4 for AC-25, and 2.2 for AC-35. In addition, the FWHM of the D-mode for AC-25 and AC-35 are increased comparing to AC and AC-15 (101 cm^{-1} for AC, 103 cm^{-1} for AC-15, 121 cm^{-1} for AC-25, and 108 cm^{-1} for AC-35). Increasing I_D/I_G ratios as well as increasing FWHM indicate that the number of defects in hexagonal rings increases when coated with titania. Due to the oxidative reaction on the surface of the AC, carbon is partially removed, and the dangling bonds may serve as nucleation centers of the titania formation.

As seen in Fig. 3B, the Raman spectra of AC-25 and AC-35 show anatase-type nanocrystalline titania at 150 cm^{-1} [72,73]. Further characteristic anatase peaks above 400 cm^{-1} (see Ref. [74]) were not observed in our study because of the high disorder/small domain size and the high signal strength of the carbon material [75]. The well resolved E_g mode at 150 cm^{-1} (FWHM = 31 cm^{-1}) of AC-25 and AC-35 can be used to estimate the anatase domain size to be below 4 nm [74], which is in good agreement with the TEM observations (Fig. 1F, H). No anatase related Raman signals were found for AC-15 due to its low crystallinity/very small domain size resulting in very broad and overlapping peaks, making the spectrum indistinguishable from the carbon signal [75]. The incompletely crystalline nature of titania in AC-15 is also in alignment with the TEM images seen in Fig. 1D and the results in previous work [74]. It is obvious that the structure of the anatase phase is dependent on the amount coated on the carbon substrate. For very low amounts (AC-15) the titania coating starts to grow in an incompletely crystalline manner and further crystallizes to nanoscopic grains for higher loadings (AC-25). X-ray diffraction also confirms the presence of anatase, yet only for the sample with the highest titania mass loading (AC-35; Fig. 3C–G). This aligns with the high degree of disorder (esp. for AC-35) and the very small domain size (esp. for AC-15 and AC-25) when using XRD, which, as a diffraction technique, has a preferred sensitivity towards large, highly ordered scattering domains. For AC-35, we see the clear emergence of the (101) peak of anatase at 25.2° 2θ.
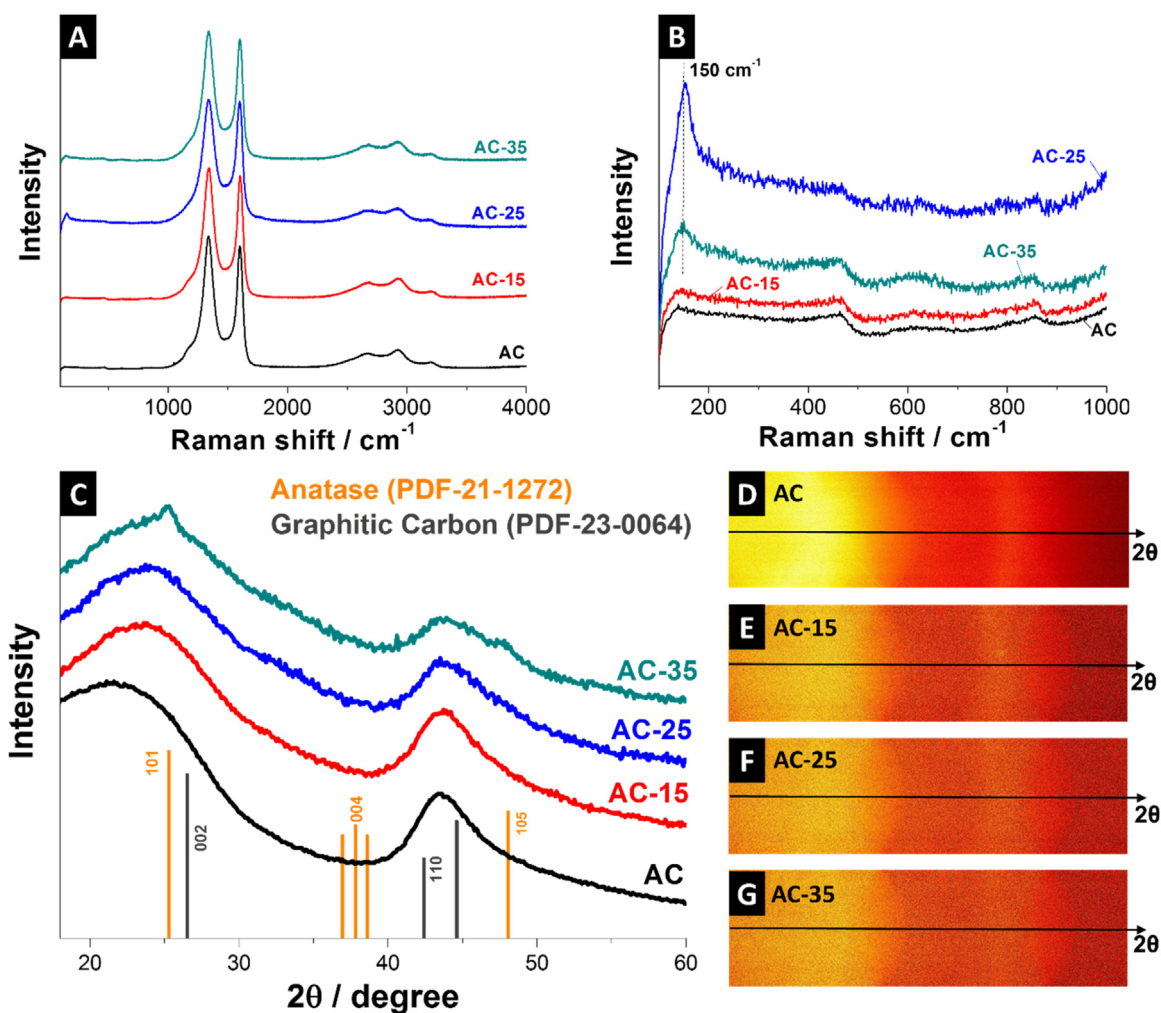
Fig. 3. Raman spectra of AC, AC-15, AC-25 and AC-35 showing the (A) full range and (B) just the range between 100–1000 cm^{-1} (i.e., range with Raman active modes of titania). (C) X-ray diffractograms of AC and AC-titania composite. The ideal peaks position from the powder diffraction files for graphitic carbon (PDF-23-0064) and anatase-type titania (PDF-21-1272) are given. (D-G) Corresponding 2D frames from the 2D detector (covering the same range in 2θ).

3.2. Electrochemical characterization in high salinity aqueous electrolyte

In aqueous CDI processes, dissolved oxygen typically shows a strong impact on cell performance, especially on the aging stability [35]. It has been proposed previously that dissolved oxygen can electrochemically react with the carbon electrode to form oxygen containing surface functional groups [76,77]. These surface functionalities affect the salt adsorption capacity by introducing local (chemical) surface charges [78,79]. To explore the potential of a metal oxide coating to mitigate the performance fading due to electrode oxidation, we tested the AC/titania hybrids as electrodes in a CDI cell. Electrosorption experiments were performed in de-aerated 1 M NaCl solution to evaluate the specific capacitance of the fabricated electrodes. As seen in Fig. 4A, the CV curve at 5 $mV\,s^{-1}$ shows typical behavior of an electric double-layer capacitor material with a rectangular shape [80]. Since no redox peaks are observed, titania in the hybrid material did not introduce any non-capacitive or non-pseudocapacitive behavior. This is underlined by galvanostatic charge-discharge measurements at 0.1 $A\,g^{-1}$ (Fig. 4B) with a triangular shape.
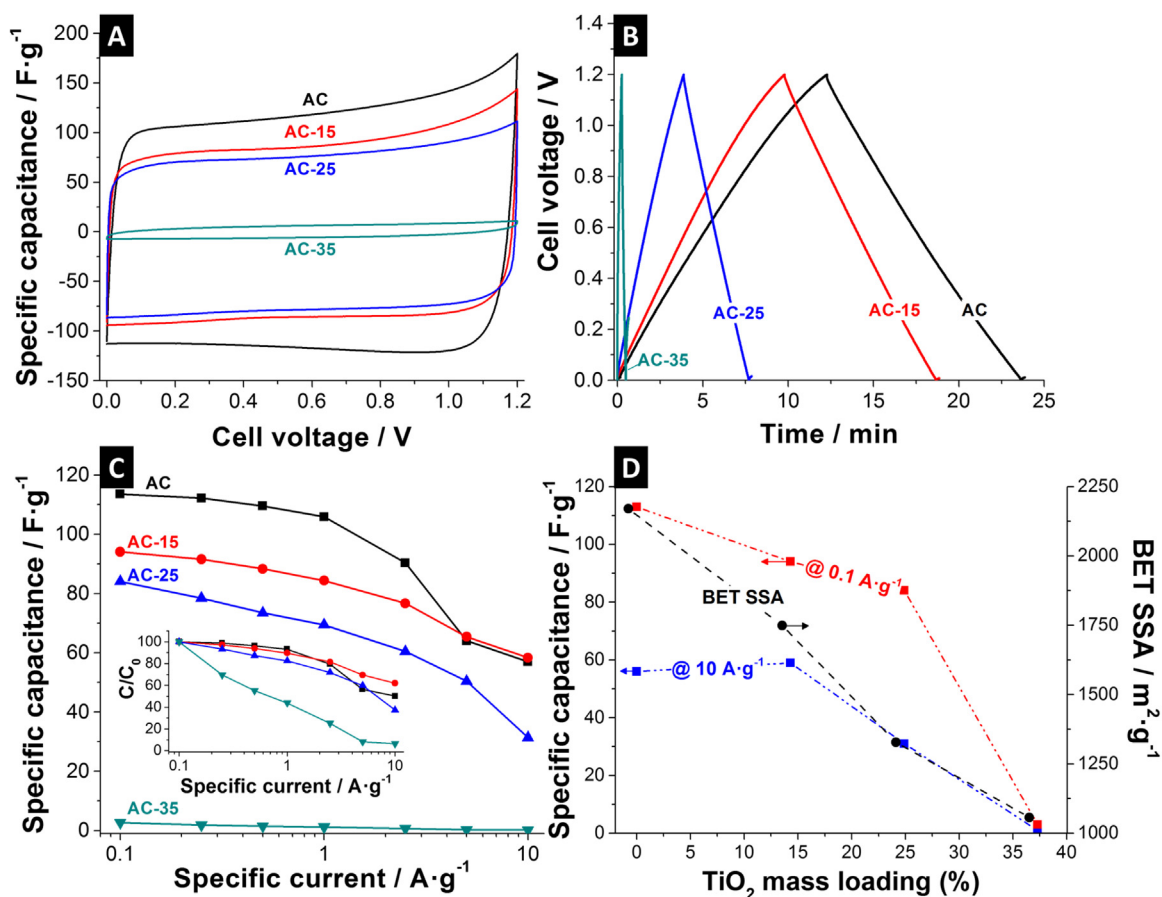
The specific capacitances from galvanostatic measurements are plotted in Fig. 4C. At a low current density of 0.1 $A\,g^{-1}$, AC exhibits the highest specific capacitance of 113 $F\,g^{-1}$, whereas AC-15, AC-25 and AC-35 show lower specific capacitances of 94 $F\,g^{-1}$, 84 $F\,g^{-1}$, and 3 $F\,g^{-1}$, respectively. As shown by nitrogen gas sorption (Fig. 2B–D), the pores of the AC are clogged by the additional titania coating. Thus, the lower accessible pore volume leads to lower specific capacitance values. The decrease in capacitance is further

amplified by the mass increase cause by the addition of electrochemically inactive titania (Fig. 4D).

3.3. Capacitive deionization performance

To evaluate the salt adsorption performance under realistic conditions, we tested the as-assembled CDI cell under saturated O_2 in 5 mM NaCl (Fig. 5). As shown in Fig. 5A, AC and all hybrid electrodes exhibit a distinct salt adsorption and desorption behavior in the first three cycles. This behavior is changing significantly after 20 cycles, as the AC electrodes show a strong desorption peak before the onset of the adsorption (Fig. 5B). The latter feature, also referred to as an inversion peak, has been observed previously [20,32], and is attributed to the oxidation of the positive electrode and the consequential increase in the concentration of negatively charged surface functional groups in the micropores [23,25,26]. Post mortem EDX analysis (Fig. 5D) was carried out to give further evidence of additional oxygen-containing surface modifications. The electrodes were cycled in oxygen saturated 5 mM NaCl for 40 cycles and the positive and negative electrodes were chemically analyzed separately. We observed that after cycling, the oxygen content of the positive electrode (14.8 ± 3.3 mass%) was more than three-times higher than the negative electrode (4.4 ± 0.6 mass%), strongly indicating the formation of oxygen containing surface functional groups.

Hybrid electrodes with titania show a similar behavior [41,81], but with a much smaller inversion peak for AC-15, which vanishes entirely for electrodes with higher titania loadings (Fig. 5B). The

Fig. 4. (A) Cyclic voltammograms at 5 $mV\,s^{-1}$, (B) galvanostatic charge-discharge curves at 0.1 $A\,g^{-1}$, (C) specific capacitance versus specific current, and (D) specific capacitance and BET SSA plotted against the titania mass loading for high and low rates. All electrodes are free-standing PTFE-bond electrodes.
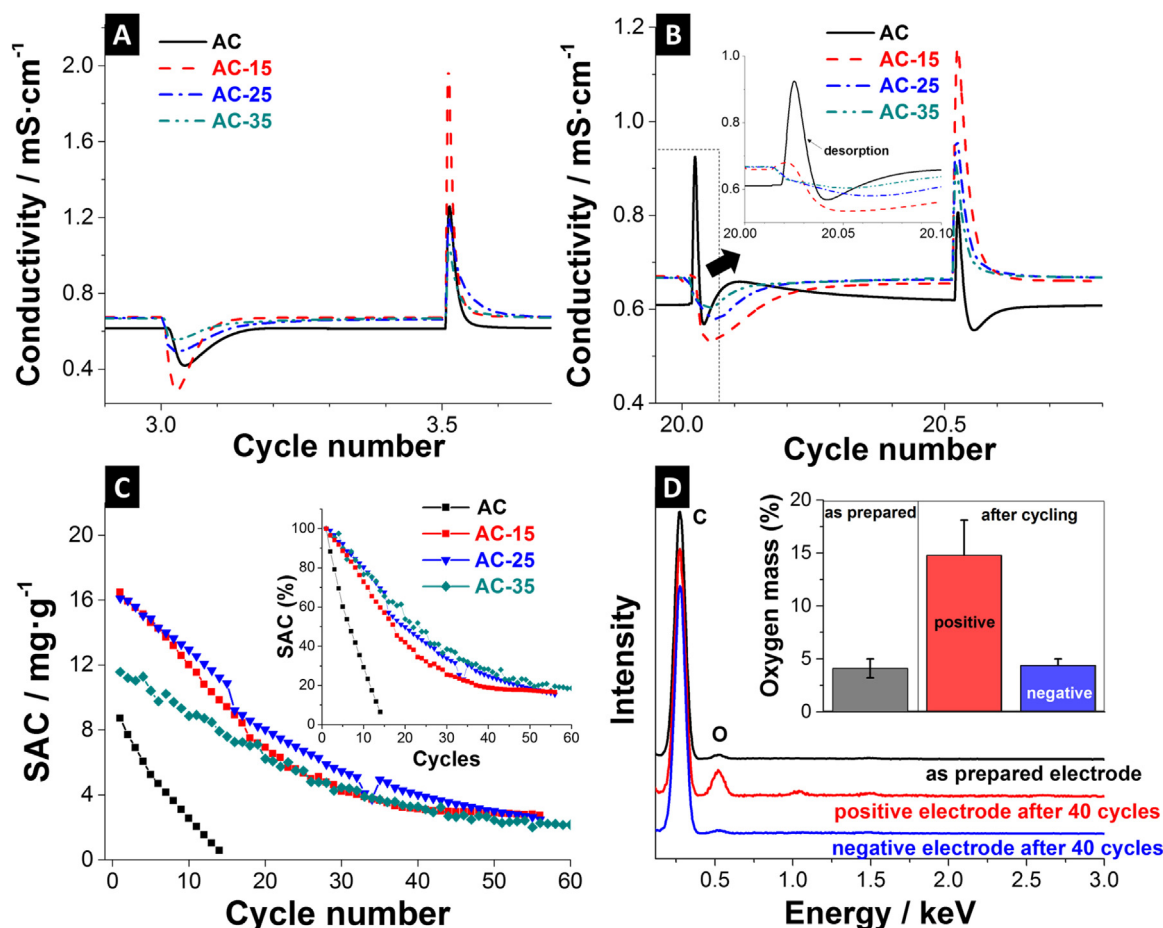
Fig. 5. CDI performance in oxygen saturated 5 mM NaCl at 1.2 V using free-standing PTFE-bond electrodes. Conductivity data of the outlet flow stream for (A) 3rd and (B) 20th cycle. (C) Salt adsorption capacity for 60 cycles and (D) EDX analysis of PVP/PVB-bound positive and negative electrodes after 40 desalination cycles with 5 mM oxygen saturated NaCl electrolyte at 1.2 V.

measured salt adsorption capacities exhibit values of 17.4 mg g^{-1} and 16.2 mg g^{-1} for AC-15 and AC-25, respectively, whereas AC-35 shows a smaller SAC of 11.4 mg g^{-1}. In comparison, the AC electrodes have the lowest SAC of around 9 mg g^{-1}. Earlier works (Table 4) had already reported an enhanced SAC for metal oxide/carbon hybrids (in particular titania/carbon hybrids) [55–59]. Enhanced wettability has been proposed as a cause of the improvements in the SAC of the hybrid material [39,82], and micropore surface groups may also play a role [83]. Interestingly, the measured SAC of titania containing electrodes does not follow the same general trend of the measured capacitance of the electrodes determined by galvanostatic charge/discharge experiments in oxygen-free 1 M NaCl (Fig. 4D).

As shown in Fig. 5C, the CDI performance of AC is significantly improved in oxygen saturated aqueous media by addition of titania in the first cycles. The titania containing electrodes show a much slower decrease of SAC with ∼50 % of the initial SAC after 20 cycles and ∼20% after 60 cycles. While titania decoration did not fully prevent the performance degradation, there is still a remarkable performance and stability enhancement clearly visible for carbon/metal oxide hybrids. The SAC of all titania containing samples converges at ca. 2 mg g^{-1} after 60 cycles and this value seems to remain rather constant irrespective of the used amount of titania. This is in stark contrast to AC samples without titania, where the entire CDI salt removal capacity is readily lost completely after 15 cycles.

For pure AC, the performance in de-aerated 5 mM NaCl is shown in Fig. S4 (*Supplementary Information*). For this electrolyte, a high SAC of ca. 13 mg g^{-1} is maintained over 40 full CDI cycles (Fig. S4C, *Supplementary Information*), which is in stark contrast to the performance loss in oxygen saturated electrolyte with a virtually complete loss of the desalination capacity after just 15 cycles. The difference in performance stability is also seen from assessing the charge efficiency, as depicted in Fig. S4D (*Supplementary Information*). In de-aerated saline solution, the charge efficiency of AC remains constant at ca. 71% which is indicative of a highly reversible process of co-ion expulsion and counter-ion adsorption. For comparison, the charge efficiency of AC in oxygen saturated solution is much lower at 34% in the first cycle and fades to 0% after 15 cycles. This is in line with previous reports on the increased electrochemical degradation of carbon electrodes by dissolved oxygen [34].

To get more information on the impact of prolonged CDI cycling on AC containing titania electrodes, the potential development of the CDI cycled electrodes was benchmarked by galvanostatic charge/discharge testing at 0.1 A g^{-1} for fresh electrodes and after CDI cycling. The potential evolution of the cathode and the anode for AC-15 and AC-25 is very similar before and after CDI cycling (Fig. S6A,*Supplementary Information*). In both cases, we see a shift of the cell potential to +0.23 V vs. Ag/AgCl compared to fresh electrodes. As seen in Fig. S6A-B, after 60 cycles of CDI experiment, the symmetric AC-15 and AC-25 cells already exceed the theoretical oxygen evolution

potential at a cell voltage of 0.6 V. Hence, the anode is the limiting electrode. At a cell voltage of 1.2 V, AC-15 and AC-25 exhibit a potential that is 0.2 V higher than the theoretical oxygen evolution potential. AC-35 exhibits a similar cathodic and anodic potential as fresh electrodes, but the zero charge potential at a cell voltage of 1.2 V is shifted to 0.15 V vs. Ag/AgCl after 60 CDI cycles (Fig. S6C-D, *Supplementary Information*). This leads to an asymmetric potential distribution between cathode (ΔE ca. 0.8 V at cell voltage 1.2 V) and anode (ΔE ca. 0.4 V at cell voltage 1.2 V). This positive shifting might affect the SAC through lower accumulation of charges on the positive electrode, causing the anode to limit the total salt adsorption of the cell.

Charge efficiency, the ratio between invested charge and removed ions, is a useful tool to further characterize CDI performance and stability [21]. As shown in Fig. 5D (*Supplementary Information*), the charge efficiency of all titania containing samples is nearly three-fold higher than for pure AC at the first cycle. All three composite electrodes maintain a high charge efficiency between 90 % and 100 % for ca. 10 cycles and then gradually decrease to ca. 20 % after 60 cycles. Such high initial values for the charge efficiency cannot be explained by a pure EDL formation and ion swapping, as we see much lower values for pure AC in oxygen saturated electrolyte (Fig. S4D, *Supplementary Information*). Thereby, an electron uptake of dissolved oxygen from the cathode and the resulting effect on the SAC and charge efficiency through a Faradaic ORR is confirmed. Thus, it is indicated that the introduction of Faradaic oxygen reduction seems to have a significant impact.

3.4. ORR activity measurements

To investigate the oxygen reduction reactions (ORR) of the hybrid electrodes with different quantities of titania, cyclic voltammetry was carried out at 5 mV s^{-1} in de-aerated and in oxygen saturated 1 M NaCl. The results of these measurements are shown in Fig. 6. It was found that the CV of AC in de-aerated solution is rectangular, as it is typical for systems with purely capacitive behavior and without any Faradaic contributions (Fig. 6A). In the case of oxygen saturated electrolyte, a well-defined ORR onset potential is observed at 16 mV vs. Ag/AgCl. The results of AC-titania hybrid samples in de-aerated media are like those of AC, but with lower specific current and less potential window stability (Fig. 6). Higher mass loadings of titania lead to a lower electrochemical potential for hydrogen evolution reactions (HER) and, in turn, to a lowered applicable potential. Especially, AC-35 shows comparably low potential window stability, because the nanocrystallinity of titania favors HER [50]. In the O$_2$ saturated solution, ORR peaks for titania hybrid electrodes (AC-15, AC-25 and AC-35) are appearing at the onset potential of +46 mV, −38 mV, and −21 mV vs. Ag/AgCl, respectively. Typically, for reduction potentials closer to the standard potential of oxygen reduction (between +170 mV and −360 mV vs. Ag/AgCl depending on the mechanism) [84], the oxygen reduction reaction is favorable.
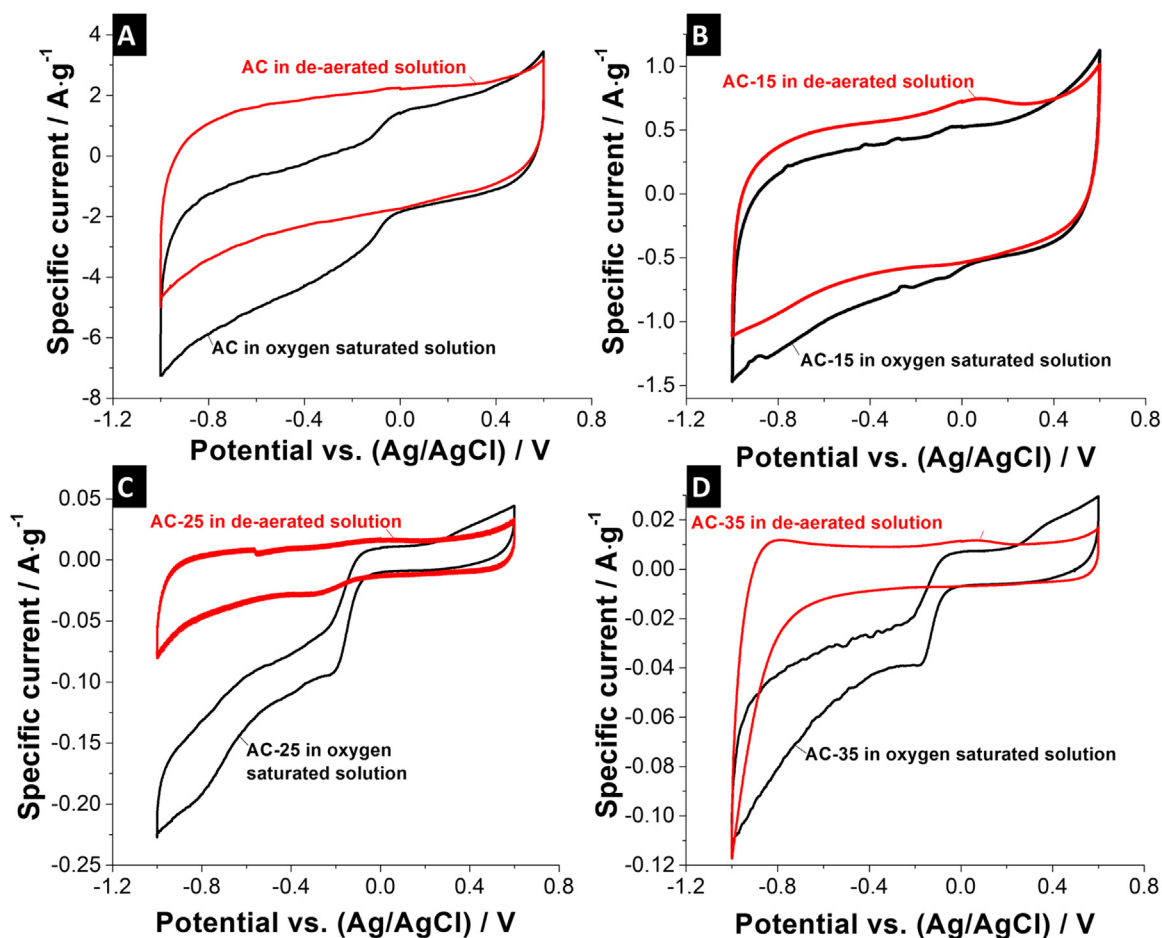

Fig. 6. Cyclic voltammograms in de-aerated and oxygen saturated aqueous 1 M NaCl at 5 mV s^{-1} for (A) AC, (B) AC-15, (C) AC-25, and (D) AC-35.

Table 3

Density and specific resistivity of film electrodes. Film electrodes were prepared by rolling of activated carbon and AC-titania mixtures with different amounts of PTFE binder (film thickness: 180-200 μm).

Sample name	PTFE binder (mass%)	Electrode density (g cm^3)	Specific resistivity (ohm cm)
AC	5.0	0.42 ± 0.03	9 ± 1
AC-15	5.0	0.52 ± 0.02	18 ± 2
AC-25	7.5	0.60 ± 0.03	86 ± 7
AC-35	10.0	0.72 ± 0.05	>2000

Among all samples, AC-15 shows the highest ORR potential of +46 mV vs. Ag/AgCl, indicating a stronger oxygen reduction tendency. The onset reduction potentials of the hybrid electrodes AC-25 and AC-35 are more negative than the AC electrodes; this can be understood as an impeded ORR due to a lower accessibility of the carbon, as well as a reduced electrical conductivity (Table 3) due to the rather thick titania coating.

In Fig. 7A, B, the intrinsic ORR currents of AC and hybrid electrodes are calculated by subtracting the current in oxygen saturated electrolyte by the capacitive current in de-aerated electrolyte. When using just AC, we see a simultaneous increase of the specific ORR current as the potential becomes more negative from 16 mV to -400 mV vs. Ag/AgCl. This is commonly observed for metal-free ORR catalysts [85]. For comparison, AC-15 exhibits the same phenomenon as AC, but with a lower (more positive) ORR specific current, suggesting synergistic ORR activity between AC and titania. AC-25 and AC-35 show different ORR activities compared to AC and AC-15, with a sharp step in the specific current from the onset potential (-48 mV and -21 mV vs Ag/AgCl) to a certain potential (-220 mV and -200 mV vs. Ag/AgCl), before the constant plateau occurs (Fig. 7A, B). The plateau current demonstrates that the reaction at this scan rate (5 mV s^{-1}) is diffusion limited [86]. This suggests an impeded diffusion of oxygen species due to a faster transfer of the first electron, which is more pronounced for higher loadings.

A technique to measure the reaction rate of oxygen species on the active surface involves the Tafel equation and the Tafel slope [87]. The Tafel equation (Eq. (2)) is derived from the Butler-Volmer equation [88,89] and is typically a logarithmic plot of the current i versus the overpotential η, which should be linear at each rate of reaction. The ORR kinetics are obtained from the slope of the Tafel

plot via Eq. (2):

$$\log i = \log i_0 - \frac{\alpha nF}{RT}\eta \qquad (2)$$

where, i_0 is the exchange current, α is the charge transfer coefficient, F is Faraday's constant (96485 C mol^{-1}), R is the ideal gas constant (8.314 J mol^{-1} K^{-1}), T is the temperature (296 K), and n is number of electron transfers.

As shown in Fig. 7C, the cathodic Tafel plot of all samples exhibits two different slopes: one at low overpotential and one at high overpotential. At low overpotential, the rate-determining step is the first electron transfer leading to oxygen reduction, while at the higher over potential, the kinetics are limited by oxygen diffusion [90]. The calculated Tafel slopes for both potentials are displayed in Fig. 7D. AC-15 shows a low overpotential Tafel slope higher than AC due to multiple steps of reduction processes of the titania. For high titania loadings (i.e., AC-25 and AC-35), the catalytic activity is dominated by titania. Hence, titania might reduce oxygen in different pathways. The Tafel slopes at high overpotential increase with higher amounts of titania, potentially because of the poor conductivity (sluggish electron flow rate), as well as the diffusion limitations of oxygen (pore blocking by titania coating) within the AC-titania hybrid

In summary, AC and AC-15 show higher rates of ORR than AC-25 and AC-35 at high overpotentials, while the two latter achieve higher rates of ORR at low overpotential due to the strong influence of titania. Figs. 6 and 7 clearly show the catalytic ability for AC and AC-titania hybrids. However, the mechanism of such a reaction needs to be studied in more detail, since there are different possible ORRs between carbon and metal oxide, which can affect the CDI performance (Supporting Information equations S1-S9).

The formation of surface functional groups is a particularly critical issue affecting the aging of CDI electrodes. It is expected that, during CDI operation, H_2O_2 is formed through the reduction of oxygen in the solution, and the H_2O_2 then oxidizes the positive electrode (Fig. 5D) [35,91]. Thus, to understand the ORR, several reaction steps have to be considered, which are either a direct 4 electron pathway (Eq. (3)) or a two-step two-electron pathway (Eqs. (4)–(5)) [25,92]. Following a perfect ORR four-electron pathway, O_2 directly reacts on the surface of the carbon and forms hydroxyl ions. In the two-step, two-electron pathway, peroxide ions are formed in an intermediate step (Eq. (4)) and then peroxide

Table 4

Comparison of salt adsorption capacity (SAC) of metal oxide-carbon composite.

| Samples	Salt concentration	SAC	Charge efficiency	Operation voltage	Ref.
ZrO$_2$/graphene oxide	50 mg L^{-1}	4.5 mg g^{-1}	93%	1.2 V	[97]
TiO$_2$/CNTs	25-800 mg L^{-1}	4 mg g^{-1}	na.	1.4 V	[39]
TiO$_2$/AC	5-560 mg L^{-1}	21 mg g^{-1}	na.	0.3-1.2 V	[40]
TiO$_2$/AC	5.8 mg L^{-1} 0.1 mM	0.5 mg g^{-1}	na.	1 V	[41]
MnO$_2$/MWCNTs	87 mg L^{-1}	6.6 mg g^{-1}	na.	1.8 V	[98]
TiO$_2$ nanorod/rGO	300 mg L^{-1}	9.1 mg g^{-1}	50 %	1.2 V	[82]
TiO$_2$ nanofiber/AC	292 mg L^{-1}	17.7 mg g^{-1}	90 %	1.2 V	[99]
ZnO/AC	500 mg L^{-1}	9.4 mg g^{-1}	80.5 %	0.4-1.5 V	[36]
SnO$_2$/rGO	na.	1.5 mg g^{-1}	80 %	1.4 V	[38]
MnO$_2$/rGO	56000 mg L^{-1}	5 mg g^{-1}	93 %	1.2 V	[100]
MnO$_2$/AC	35 mg L^{-1}	9.4 mg g^{-1}	81 %	1.2 V	[37]
TiO$_2$/rGO	1400 mg L^{-1}	17.8 mg	na.	1.8 V	[101]
TiO$_2$/AC	100 mg L^{-1}	11.5 mg g^{-1}	na.	1.2 V	[102]
AC-15	280 mg L^{-1}	17.4 mg g^{-1} ca.2 mg g^{-1} after 60 cycles	22% after 60 cycles	1.2 V	This work
AC-25	280 mg L^{-1}	16.2 mg g^{-1} ca.2 mg g^{-1} after 60 cycles	22% after 60 cycles	1.2 V	This work
AC-35	280 mg L^{-1}	11.4 mg g^{-1} ca. 2 mg g^{-1} after 60 cycles	22% after 60 cycles	1.2 V	This work
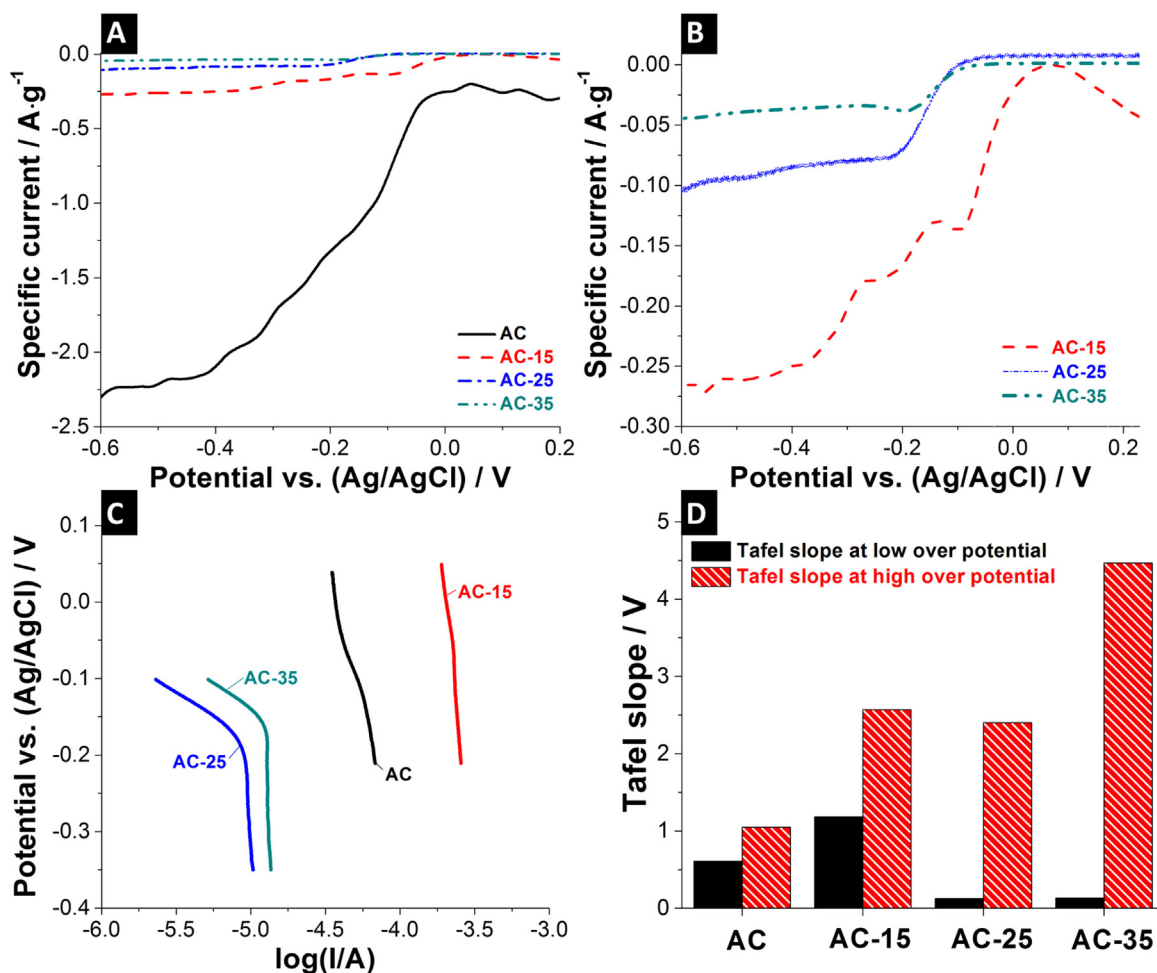
Fig. 7. (A, B) Intrinsic ORR currents at $5\,mV\,s^{-1}$, (C) Tafel plot, and (D) Tafel slopes of AC, AC-15, AC-25, and AC-35.

ions form the hydroxyl ions (Eq. (5)). However, peroxide ions in the intermediate steps cannot further be reduced due to their high reduction potential, so that the direct four electron pathway without peroxide formation would be preferable with respect to suppress the oxidation of carbon electrodes.

$$O_2 + 2H_2O + 4e^- \rightarrow 4OH^- \tag{3}$$

$$O_2 + H_2O + 2e^- \rightarrow HO_2^- + OH^- \tag{4}$$

$$HO_2^- + H_2O + 2e^- \rightarrow 3OH^- \tag{5}$$

Hence, to see which ORR reactions takes place, the electrodes were further evaluated at various scan rates, to get further insight into the relation between the rate of electron transfer and oxygen diffusion. As can be concluded from the Tafel slope (Fig. 7D), the rate limiting step is the bulk diffusion of dissolved oxygen. To reduce such influence, the increase of the sweep rate enhances the ORR kinetics in terms of acceleration of the charge transfer. For each scan rate, the specific ORR current was calculated as described in the last section. It can clearly be observed that the diffusion-limiting specific current of AC increases with the scan rate in the range from $-0.15\,V$ to $-0.2\,V$ vs. Ag/AgCl, suggesting that the charge transfer rate of AC is increased at high rates and more oxygen is reduced (Fig. 8A). In addition, the peaks appeared more clearly after the scan rate is increased up to $20\,mV\,s^{-1}$ (Fig. 8A). For AC-15, we could observe complementary behavior with the

specific peak current disappearing when the sweep rate is increased (Fig. 8B). For low scan rates, the rate of charge transfer at the solid/liquid interface is lower than for high scan rate. With higher scan rates, the ORR kinetics are increased to reach the equilibrium between rate of electron transfer and rate of oxygen diffusion as indicated by the absence of a peak at a high scan rate ($50\,mV\,s^{-1}$). In case of AC-25 and AC-35 (Fig. 8C, D), the specific currents exhibit plateaus for low scan rates ($5\,mV\,s^{-1}$) indicating the reaction reaches equilibrium. For higher rates, peaks appear since the surface reaction of titania is much faster than bulk diffusion of oxygen. This is especially seen for AC-35, where most the pores are blocked by titania. The number of transferred electrons, which indicates the specific ORR pathway, can be calculated with the Randles-Sevcik equation (Eq. (6)) [93,94]:

$$i_p = (2.99 \cdot 10^5) n(n\alpha)^{0.5} ACD^{0.5} \nu^{0.5} \tag{6}$$

A is the active surface area (in this case: DFT-SSA), C is the concentration of dissolved oxygen ($2.59 \cdot 10^{-7}\,mol\,cm^{-2}$) [95], D is the diffusion coefficient of oxygen ($2 \cdot 10^{-5}\,cm^2\,s^{-1}$), α is the charge transfer coefficient, n is number of electron transfers and ν is the scan rate. The term $n\alpha$ is calculated from the Tafel slope at high potential using Eq. (7) [87]:

$$Tafel\,slope = \frac{2.303 \cdot RT}{\alpha n F} \tag{7}$$

The reduction currents at the peak maximum are plotted versus the square root of scan rate as shown in Fig. 8E. It was found that AC, AC-15, AC-25 and AC-35 present slopes of -0.056, -0.664, -0.062,
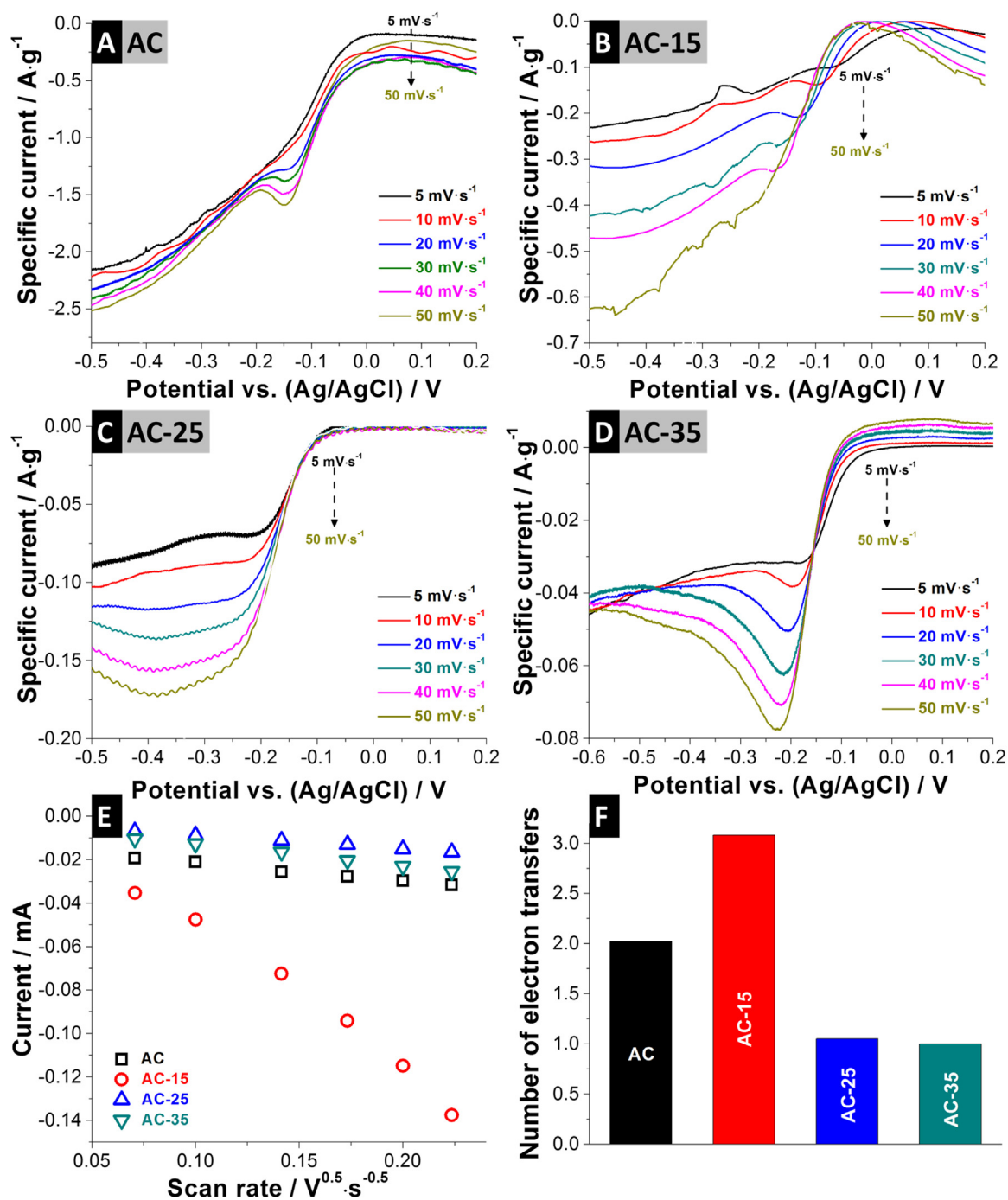
Fig. 8. Intrinsic ORR specific currents at different scan rates for (A) AC, (B) AC-15, (C) AC-25, and (D) AC-35. (E) ORR peak currents versus square root of scan rate, and (F) number of electron transfers.

and $-0.101\,mA\,(V\,s^{-1})^{0.5}$, respectively. The number of electron transfers is calculated and plotted in Fig. 8F. AC without additional catalyst exhibits an electron transfer of 2.02, indicating a two-electron oxygen reduction reactions takes place, in which hydrogen peroxide ions are produced (Eq. (4)) [76,77]. Hydrogen peroxide strongly oxidizes the carbon surface leading to the formation of oxygen containing surface groups [78]. These functional groups create local negative charges at the positive electrode, which cause the inverse peak during the adsorption process (Fig. 5B). This verifies that during CDI operation and in the presence of oxygen in the electrolyte, hydrogen peroxide plays a crucial role at the positive electrode resulting in poor aging performance [35,96].

The catalytic role of titania during the CDI process shows different ORR mechanisms (number of electron transfers) dependent on the mass loading. As we can see in Fig. 8F, AC-15 shows the highest electron transfer of 3.08, whereas AC-25 and AC-25 show 1.05 and 1.01 electron transfers, respectively. The different mechanisms regarding the number of electron transfers of the hybrid materials can protect the oxidation of carbon at the positive electrode in different ways [49]:

• For AC-25 and AC-35, a single electron transfer is indicated due to the higher activation energy barrier leading to catalyst poisoning and incomplete reactions. Per the mechanism shown in Fig. S3

(*Supplementary Information*), the dissolved oxygen adsorbs on the titania surface and the first electron reacts with it to form superoxide. The latter strongly adsorbs on active sites which are used to transform oxygen to superoxide. Over the time, the active sites of titania are blocked and cannot be further used for ORR. Therefore, using AC-25 and AC-35 in CDI results in a continuous decrease of the SAC (Fig. 5C) because of active site blockage and the formation of hydrogen peroxide, which strongly oxidizes the carbon surface.

- In case of AC-15, 3.08 electron transfers are indicated. This could be explained by the following ORR mechanism, schematically shown in Fig. S3 (*Supplementary Information*). First, oxygen diffuses and selectively adsorbs on the surface of titania. Once an electrical potential is applied on AC-15, the first electron will react with oxygen to form superoxide. Afterwards, the second electron reacts with superoxide and water to generate hydroxyl ions and peroxide. The third electron, then, reacts with the peroxide and the water producing hydroxide and hydroxyl radicals. However, hydroxyl radicals should further be reduced to form hydroxyl ions in a perfect 4-electron process, but AC-15 presents only three-electron transfers. Therefore, hydroxyl radicals adsorb on the active site of titania and when the entire surface is blocked, the ORR cannot proceed. Hence, the SAC of AC-15 will be decreased and becomes constant at 20 % of the initial SAC after 60 cycles (Fig. 5C).

4. Conclusions

We have provided a comprehensive study on the advantages of AC-titania hybrids for the CDI performance in oxygen saturated saline water (5 mM NaCl). AC-titania hybrids were successfully prepared by a sol-gel method resulting in different mass loadings of titania. It was found that higher amounts of titania lead to reduced surface areas due to pore blocking by the titania coating and thus, to lower specific capacitances measured in de-aerated electrolyte. Interestingly, CDI measurements present a contra- dicting behavior in O_2-saturated NaCl with higher SACs for the titania coated samples and better long-time stability. For example, a 15 mass% loading of titania results in $\sim$17.4 mg g^{-1} SAC in the first cycles compared to AC with an initial value of $\sim$9 mg g^{-1}. After 15 cycles, the AC-15 hybrid demonstrates a comparably high SAC of more than $\sim$8 mg g^{-1} (about 50 % of the initial value), while the SAC of AC decreases to zero. Pure AC exhibits poor catalytic activity for oxygen reduction in a two-electron transfer, so that the carbon electrode is oxidized by hydrogen peroxide and surface functional groups are formed. In contrast, AC-15 leads to a three-electron transfer reaction which impedes the formation of hydrogen peroxide and partially prevents the carbon electrode from oxidizing. With this approach, higher SACs, as well as better cycling stability can be reached. Yet, the strong decay of SAC over cycles remains a challenge to be overcome and the full potential of the carbon/metal oxide is yet to be shown.

Acknowledgements

Appendix A. Supplementary data

Supplementary data associated with this article can be found, in the online version, at http://dx.doi.org/10.1016/j.electacta.2016.12.060.

References

[1] T.Y. Cath, A.E. Childress, M. Elimelech, Forward osmosis: Principles, applications, and recent developments, Journal of Membrane Science 281 (2006) 70–87.

[2] M. Elimelech, W.A. Phillip, The Future of Seawater Desalination: Energy, Technology, and the Environment, Science 333 (2011) 712–717.

[3] M.A. Shannon, P.W. Bohn, M. Elimelech, J.G. Georgiadis, B.J. Marinas, A.M. Mayes, Science and technology for water purification in the coming decades, Nature 452 (2008) 301–310.

[4] N. Savage, M.S. Diallo, Nanomaterials and Water Purification: Opportunities and Challenges, Journal of Nanoparticle Research 7 (2005) 331–342.

[5] K.P. Lee, T.C. Arnot, D. Mattia, A review of reverse osmosis membrane materials for desalination—Development to date and future potential, Journal of Membrane Science 370 (2011) 1–22.

[6] L. Alvarado, A. Chen, Electrodeionization: Principles, Strategies and Applications, Electrochimica Acta 132 (2014) 583–597.

[7] Y.S. Dzyazko, L.N. Ponomaryova, L.M. Rozhdestvenskaya, S.L. Vasilyuk, V.N. Belyakov, Electrodeionization of low-concentrated multicomponent Ni2 +-containing solutions using organic–inorganic ion-exchanger, Desalination 342 (2014) 43–51.

[8] B. Jia, W. Zhang, Preparation and Application of Electrodes in Capacitive Deionization (CDI): a State-of-Art Review, Nanoscale Research Letters 11 (2016) 1–25.

[9] S. Porada, R. Zhao, A. van der Wal, V. Presser, P.M. Biesheuvel, Review on the science and technology of water desalination by capacitive deionization, Progress in Materials Science 58 (2013) 1388–1442.

[10] Y. Oren, Capacitive deionization (CDI) for desalination and water treatment – past, present and future (a review), Desalination 228 (2008) 10–29.

[11] J.K. Ewert, D. Weingarth, C. Denner, M. Friedrich, M. Zeiger, A. Schreiber, N. Jackel, V. Presser, R. Kempe, Enhanced capacitance of nitrogen-doped hierarchically porous carbide-derived carbon in matched ionic liquids, Journal of Materials Chemistry A 3 (2015) 18906–18912.

[12] S. Porada, F. Schipper, M. Aslan, M. Antonietti, V. Presser, T.-P. Fellinger, Capacitive Deionization using Biomass-based Microporous Salt-Templated Heteroatom-Doped Carbons, ChemSusChem 8 (2015) 1867–1874.

[13] C. Prehal, D. Weingarth, E. Perre, R.T. Lechner, H. Amenitsch, O. Paris, V. Presser, Tracking the structural arrangement of ions in carbon supercapacitor nanopores using in situ small-angle X-ray scattering, Energy & Environmental Science 8 (2015) 1725–1735.

[14] P.M. Biesheuvel, S. Porada, M. Levi, M.Z. Bazant, Attractive forces in microporous carbon electrodes for capacitive deionization, Journal of Solid State Electrochemistry 18 (2014) 1365–1376.

[15] M.E. Suss, S. Porada, X. Sun, P.M. Biesheuvel, J. Yoon, V. Presser, Water desalination via capacitive deionization: what is it and what can we expect from it? Energy & Environmental Science 8 (2015) 2296–2319.

[16] Y.-J. Kim, J.-H. Choi, Enhanced desalination efficiency in capacitive deionization with an ion-selective membrane, Separation and Purification Technology 71 (2010) 70–75.

[17] P.M. Biesheuvel, A. van der Wal, Membrane capacitive deionization, Journal of Membrane Science 346 (2010) 256–262.

[18] J. Yang, L. Zou, N.R. Choudhury, Ion-selective carbon nanotube electrodes in capacitive deionisation, Electrochimica Acta 91 (2013) 11–19.

[19] P.M. Biesheuvel, H.V.M. Hamelers, M.E. Suss, Theory of Water Desalination by Porous Electrodes with Immobile Chemical Charge, Colloids and Interface Science Communications 9 (2015) 1–5.

[20] X. Gao, S. Porada, A. Omosebi, K.L. Liu, P.M. Biesheuvel, J. Landon, Complementary surface charge for enhanced capacitive deionization, Water Research 92 (2016) 275–282.

[21] R. Zhao, P.M. Biesheuvel, H. Miedema, H. Bruning, A. van der Wal, Charge Efficiency: A Functional Tool to Probe the Double-Layer Structure Inside of Porous Electrodes and Application in the Modeling of Capacitive Deionization, The Journal of Physical Chemistry Letters 1 (2010) 205–210.

[22] I. Cohen, E. Avraham, Y. Bouhadana, A. Soffer, D. Aurbach, Long term stability of capacitive de-ionization processes for water desalination: The challenge of positive electrodes corrosion, Electrochimica Acta 106 (2013) 91–100.

[23] K.G. Gallagher, T.F. Fuller, Kinetic model of the electrochemical oxidation of graphitic carbon in acidic environments, Physical Chemistry Chemical Physics 11 (2009) 11557–11567.

[24] K.G. Gallagher, G. Yushin, T.F. Fuller, The Role of Nanostructure in the Electrochemical Oxidation of Model-Carbon Materials in Acidic Environments, Journal of The Electrochemical Society 157 (2010) B820–B830.

[25] J.-H. Lee, W.-S. Bae, J.-H. Choi, Electrode reactions and adsorption/desorption performance related to the applied potential in a capacitive deionization process, Desalination 258 (2010) 159–163.

[26] I. Cohen, E. Avraham, Y. Bouhadana, A. Soffer, D. Aurbach, The effect of the flow-regime, reversal of polarization, and oxygen on the long term stability in capacitive de-ionization processes, Electrochimica Acta 153 (2015) 106–114.

[27] F. Duan, X. Du, Y. Li, H. Cao, Y. Zhang, Desalination stability of capacitive deionization using ordered mesoporous carbon: Effect of oxygen-containing surface groups and pore properties, Desalination 376 (2015) 17–24.

[28] X. Gao, A. Omosebi, J. Landon, K. Liu, Surface charge enhanced carbon electrodes for stable and efficient capacitive deionization using inverted adsorption-desorption behavior, Energy & Environmental Science 8 (2015) 897–909.

[29] X. Gao, A. Omosebi, N. Holubowitch, A. Liu, K. Ruh, J. Landon, K. Liu, Polymer-coated composite anodes for efficient and stable capacitive deionization, Desalination 399 (2016) 16–20.

[30] R.R.A. Rios, D.E. Alves, I. Dalmázio, S.F.V. Bento, C.L. Donnici, R.M. Lago, Tailoring activated carbon by surface chemical modification with O, S, and N containing molecules, Materials Research 6 (2003) 129–135.

[31] S. Kundu, W. Xia, W. Busser, M. Becker, D.A. Schmidt, M. Havenith, M. Muhler, The formation of nitrogen-containing functional groups on carbon nanotube surfaces: a quantitative XPS and TPD study, Physical Chemistry Chemical Physics 12 (2010) 4351–4359.

[32] X. Gao, A. Omosebi, J. Landon, K. Liu, Enhanced Salt Removal in an Inverted Capacitive Deionization Cell Using Amine Modified Microporous Carbon Cathodes, Environmental Science & Technology 49 (2015) 10920–10926.

[33] B. Shapira, E. Avraham, D. Aurbach, Side Reactions in Capacitive Deionization (CDI) Processes: The Role of Oxygen Reduction, Electrochimica Acta 220 (2016) 285–295.

[34] Y. Bouhadana, E. Avraham, M. Noked, M. Ben-Tzion, A. Soffer, D. Aurbach, Capacitive Deionization of NaCl Solutions at Non-Steady-State Conditions: Inversion Functionality of the Carbon Electrodes, The Journal of Physical Chemistry C 115 (2011) 16567–16573.

[35] T. Kim, J. Yu, C. Kim, J. Yoon, Hydrogen peroxide generation in flow-mode capacitive deionization, Journal of Electroanalytical Chemistry 776 (2016) 101–104.

[36] J. Liu, M. Lu, J. Yang, J. Cheng, W. Cai, Capacitive desalination of ZnO/activated carbon asymmetric capacitor and mechanism analysis, Electrochimica Acta 151 (2015) 312–318.

[37] J. Yang, L. Zou, H. Song, Z. Hao, Development of novel MnO_2/nanoporous carbon composite electrodes in capacitive deionization technology, Desalination 276 (2011) 199–206.

[38] A.G. El-Deen, N.A.M. Barakat, K.A. Khalil, M. Motlak, H. Yong Kim, Graphene/$SnO2$ nanocomposite as an effective electrode material for saline water desalination using capacitive deionization, Ceramics International 40 (2014) 14627–14634.

[39] H. Li, Y. Ma, R. Niu, Improved capacitive deionization performance by coupling $TiO2$ nanoparticles with carbon nanotubes, Separation and Purification Technology 171 (2016) 93–100.

[40] M.-W. Ryoo, G. Seo, Improvement in capacitive deionization function of activated carbon cloth by titania modification, Water Research 37 (2003) 1527–1534.

[41] C. Kim, J. Lee, S. Kim, J. Yoon, TiO_2 sol–gel spray method for carbon electrode fabrication to enhance desalination efficiency of capacitive deionization, Desalination 342 (2014) 70–74.

[42] Y. Liang, Y. Li, H. Wang, J. Zhou, J. Wang, T. Regier, H. Dai, $Co3O4$ nanocrystals on graphene as a synergistic catalyst for oxygen reduction reaction, Nat. Mater. 10 (2011) 780–786.

[43] J. Suntivich, H.A. Gasteiger, N. Yabuuchi, H. Nakanishi, J.B. Goodenough, Y. Shao-Horn, Design principles for oxygen-reduction activity on perovskite oxide catalysts for fuel cells and metal–air batteries, Nat. Chem. 3 (2011) 546–550.

[44] F. Cheng, T. Zhang, Y. Zhang, J. Du, X. Han, J. Chen, Enhancing Electrocatalytic Oxygen Reduction on $MnO2$ with Vacancies, Angewandte Chemie International Edition 52 (2013) 2474–2477.

[45] Y. Liang, H. Wang, P. Diao, W. Chang, G. Hong, Y. Li, M. Gong, L. Xie, J. Zhou, J. Wang, T.Z. Regier, F. Wei, H. Dai, Oxygen Reduction Electrocatalyst Based on Strongly Coupled Cobalt Oxide Nanocrystals and Carbon Nanotubes, Journal of the American Chemical Society 134 (2012) 15849–15857.

[46] Z.-S. Wu, S. Yang, Y. Sun, K. Parvez, X. Feng, K. Müllen, 3D Nitrogen-Doped Graphene Aerogel-Supported Fe_3O_4 Nanoparticles as Efficient Electrocatalysts for the Oxygen Reduction Reaction, Journal of the American Chemical Society 134 (2012) 9082–9085.

[47] S. Guo, S. Zhang, L. Wu, S. Sun, Co/CoO Nanoparticles Assembled on Graphene for Electrochemical Reduction of Oxygen, Angewandte Chemie 124 (2012) 11940–11943.

[48] J. Yu, Z. Liu, L. Zhai, T. Huang, J. Han, Reduced graphene oxide supported $TiO2$ as high performance catalysts for oxygen reduction reaction, International Journal of Hydrogen Energy 41 (2016) 3436–3445.

[49] D.-N. Pei, L. Gong, A.-Y. Zhang, X. Zhang, J.-J. Chen, Y. Mu, H.-Q. Yu, Defective titanium dioxide single crystals exposed by high-energy {001} facets for efficient oxygen reduction, Nat Commun 6 (2015).

[50] J. Swaminathan, R. Subbiah, V. Singaram, Defect-Rich Metallic Titania ($TiO_{1.23}$)—An Efficient Hydrogen Evolution Catalyst for Electrochemical Water Splitting, ACS Catalysis 6 (2016) 2222–2229.

[51] A. Satyanarayana Reddy, S. Kim, H. Young Jeong, S. Jin, K. Qadir, K. Jung, C. Ho Jung, J. Yeul Yun, J. Yeong Cheon, J.-M. Yang, S. Hoon Joo, O. Terasaki, J. Young Park, Ultrathin titania coating for high-temperature stable SiO_2/Pt nanocatalysts, Chemical Communications 47 (2011) 8412–8414.

[52] D. Vorkapic, T. Matsoukas, Effect of Temperature and Alcohols in the Preparation of Titania Nanoparticles from Alkoxides, Journal of the American Ceramic Society 81 (1998) 2815–2820.

[53] C.-C. Wang, J.Y. Ying, Sol-Gel Synthesis and Hydrothermal Processing of Anatase and Rutile Titania Nanocrystals, Chemistry of Materials 11 (1999) 3113–3120.

[54] A. Matsumoto, K. Tsutsumi, K. Kaneko, Titania coating of a microporous carbon surface by molecular adsorption-deposition, Langmuir 8 (1992) 2515–2520.

[55] L. Yan, G. Chen, S. Tan, M. Zhou, G. Zou, S. Deng, S. Smirnov, H. Luo, Titanium Oxynitride Nanoparticles Anchored on Carbon Nanotubes as Energy Storage Materials, ACS Applied Materials & Interfaces 7 (2015) 24212–24217.

[56] R.B. Rakhi, W. Chen, D. Cha, H.N. Alshareef, High performance supercapacitors using metal oxide anchored graphene nanosheet electrodes, Journal of Materials Chemistry 21 (2011) 16197–16204.

[57] K. Laxman, L.A. Gharibi, J. Dutta, Capacitive deionization with asymmetric electrodes: Electrode capacitance vs electrode surface area, Electrochimica Acta 176 (2015) 420–425.

[58] M.B. Sassin, C.N. Chervin, D.R. Rolison, J.W. Long, Redox Deposition of Nanoscale Metal Oxides on Carbon for Next-Generation Electrochemical Capacitors, Accounts of Chemical Research 46 (2013) 1062–1074.

[59] M. Ramani, B.S. Haran, R.E. White, B.N. Popov, Synthesis and Characterization of Hydrous Ruthenium Oxide-Carbon Supercapacitors, Journal of The Electrochemical Society 148 (2001) A374–A380.

[60] M.-W. Ryoo, J.-H. Kim, G. Seo, Role of titania incorporated on activated carbon cloth for capacitive deionization of NaCl solution, Journal of Colloid and Interface Science 264 (2003) 414–419.

[61] S. Brunauer, P.H. Emmett, E. Teller, Adsorption of Gases in Multimolecular Layers, Journal of the American Chemical Society 60 (1938) 309–319.

[62] G.Y. Gor, M. Thommes, K.A. Cychosz, A.V. Neimark, Quenched solid density functional theory method for characterization of mesoporous carbons by nitrogen adsorption, Carbon 50 (2012) 1583–1590.

[63] M. Aslan, D. Weingarth, P. Herbeck-Engel, I. Grobelsek, V. Presser, Polyvinylpyrrolidone/polyvinyl butyral composite as a stable binder for castable supercapacitor electrodes in aqueous electrolytes, Journal of Power Sources 279 (2015) 323–333.

[64] P. Srimuk, L. Ries, M. Zeiger, S. Fleischmann, N. Jäckel, A. Tolosa, B. Krüner, M. Aslan, V. Presser, High performance stability of titania decorated carbon for desalination with capacitive deionization in oxygenated water, RSC Advances 6 (2016) 106081–106089.

[65] X. Xu, M. Wang, Y. Liu, T. Lu, L. Pan, Metal-organic framework-engaged formation of a hierarchical hybrid with carbon nanotube inserted porous carbon polyhedra for highly efficient capacitive deionization, Journal of Materials Chemistry A 4 (2016) 5467–5473.

[66] N. Jäckel, D. Weingarth, A. Schreiber, B. Krüner, M. Zeiger, A. Tolosa, M. Aslan, V. Presser, Performance evaluation of conductive additives for activated carbon supercapacitors in organic electrolyte, Electrochimica Acta 191 (2016) 284–298.

[67] Y. Wang, Y. Zou, J. Chen, G.-D. Li, Y. Xu, A flexible and monolithic nanocomposite aerogel of carbon nanofibers and crystalline titania: fabrication and applications, RSC Advances 3 (2013) 24163–24168.

[68] B. Gao, G.Z. Chen, G. Li Puma, Carbon nanotubes/titanium dioxide (CNTs/$TiO2$) nanocomposites prepared by conventional and novel surfactant wrapping sol–gel methods exhibiting enhanced photocatalytic activity, Applied Catalysis B: Environmental 89 (2009) 503–509.

[69] M. Aslan, M. Zeiger, N. Jäckel, I. Grobelsek, D. Weingarth, V. Presser, Improved capacitive deionization performance of mixed hydrophobic/hydrophilic activated carbon electrodes, Journal of Physics: Condensed Matter 28 (2016) 114003.

[70] S. Fleischmann, N. Jäckel, M. Zeiger, B. Krüner, I. Grobelsek, P. Formanek, S. Choudhury, D. Weingarth, V. Presser, Enhanced Electrochemical Energy Storage by Nanoscopic Decoration of Endohedral and Exohedral Carbon with Vanadium Oxide via Atomic Layer Deposition, Chemistry of Materials 28 (2016) 2802–2813.

[71] A.C. Ferrari, J. Robertson, Interpretation of Raman spectra of disordered and amorphous carbon, Physical Review B 61 (2000) 14095–14107.

[72] Y. Xu, H. Lin, L. Li, X. Huang, G. Li, Precursor-directed synthesis of well-faceted brookite TiO_2 single crystals for efficient photocatalytic performances, Journal of Materials Chemistry A 3 (2015) 22361–22368.

[73] T.A. Kandiel, A. Feldhoff, L. Robben, R. Dillert, D.W. Bahnemann, Tailored Titanium Dioxide Nanomaterials: Anatase Nanoparticles and Brookite Nanorods as Highly Active Photocatalysts, Chemistry of Materials 22 (2010) 2050–2060.

[74] W.F. Zhang, Y.L. He, M.S. Zhang, Z. Yin, Q. Chen, Raman scattering study on anatase TiO_2 nanocrystals, Journal of Physics D: Applied Physics 33 (2000) 912.

[75] Y.-H. Zhang, C.K. Chan, J.F. Porter, W. Guo, Micro-Raman Spectroscopic Characterization of Nanosized $TiO2$ Powders Prepared by Vapor Hydrolysis, Journal of Materials Research 13 (1998) 2602–2609.

[76] B. Šljukić, C.E. Banks, R.G. Compton, An overview of the electrochemical reduction of oxygen at carbon-based modified electrodes, Journal of the Iranian Chemical Society 2 (2005) 1–25.

[77] R. Liu, D. Wu, X. Feng, K. Müllen, Nitrogen-Doped Ordered Mesoporous Graphitic Arrays with High Electrocatalytic Activity for Oxygen Reduction, Angewandte Chemie 122 (2010) 2619–2623.

[78] Y. Zheng, Y. Jiao, J. Chen, J. Liu, J. Liang, A. Du, W. Zhang, Z. Zhu, S.C. Smith, M. Jaroniec, G.Q. Lu, S.Z. Qiao, Nanoporous Graphitic-C_3N_4@Carbon Metal-Free Electrocatalysts for Highly Efficient Oxygen Reduction, Journal of the American Chemical Society 133 (2011) 20116–20119.

[79] R.A. Sidik, A.B. Anderson, N.P. Subramanian, S.P. Kumaraguru, B.N. Popov, O2 Reduction on Graphite and Nitrogen-Doped Graphite: Experiment and Theory, The Journal of Physical Chemistry B 110 (2006) 1787–1793.

[80] D. Weingarth, M. Zeiger, N. Jäckel, M. Aslan, G. Feng, V. Presser, Graphitization as a Universal Tool to Tailor the Potential-Dependent Capacitance of Carbon Supercapacitors, Advanced Energy Materials 4 (2014) n/a-n/a.

[81] M.W. Ryoo, G. Seo, Improvement in capacitive deionization function of activated carbon cloth by titania modification, Water Res. 37 (2003).

[82] A.G. El-Deen, J.-H. Choi, C.S. Kim, K.A. Khalil, A.A. Almajid, N.A.M. Barakat, TiO_2 nanorod-intercalated reduced graphene oxide as high performance electrode material for membrane capacitive deionization, Desalination 361 (2015) 53–64.

[83] P.B. Peters, M.Z. van Roij, P.M. Biesheuvel, Analysis of electrolyte transport through charged nanopores, Physical Review E 93 (2016) 053108.

[84] E. Yeager, Electrocatalysts for O_2 reduction, Electrochimica Acta 29 (1984) 1527–1537.

[85] J. Liang, Y. Jiao, M. Jaroniec, S.Z. Qiao, Sulfur and Nitrogen Dual-Doped Mesoporous Graphene Electrocatalyst for Oxygen Reduction with Synergistically Enhanced Performance, Angewandte Chemie International Edition 51 (2012) 11496–11500.

[86] E. Benn, J. Erlebacher, Oxygen Reduction in Nanoporous Metals Under Proton Diffusion Limited Conditions, Meeting Abstracts, MA2016-01 (2016) 1696.

[87] S.J. Clouser, J.C. Huang, E. Yeager, Temperature dependence of the Tafel slope for oxygen reduction on platinum in concentrated phosphoric acid, Journal of Applied Electrochemistry 23 (1993) 597–605.

[88] H. Geisler, A. Kromp, A. Weber, E. Ivers-Tiffée, Performance of MIEC Cathodes in SOFC Stacks Evaluated by Means of FEM Modeling, ECS Transactions 61 (2014) 191–201.

[89] J. Durst, A. Siebel, C. Simon, F. Hasche, J. Herranz, H.A. Gasteiger, New insights into the electrochemical hydrogen oxidation and evolution reaction mechanism, Energy & Environmental Science 7 (2014) 2255–2260.

[90] M. Jahan, Z. Liu, K.P. Loh, A Graphene Oxide and Copper-Centered Metal Organic Framework Composite as a Tri-Functional Catalyst for HER, OER, and ORR, Advanced Functional Materials 23 (2013) 5363–5372.

[91] Y. Peng, H. Liu, Effects of Oxidation by Hydrogen Peroxide on the Structures of Multiwalled Carbon Nanotubes, Industrial & Engineering Chemistry Research 45 (2006) 6483–6488.

[92] K. Gong, F. Du, Z. Xia, M. Durstock, L. Dai, Nitrogen-Doped Carbon Nanotube Arrays with High Electrocatalytic Activity for Oxygen Reduction, Science 323 (2009) 760–764.

[93] C.O. Laoire, S. Mukerjee, K.M. Abraham, E.J. Plichta, M.A. Hendrickson, Elucidating the Mechanism of Oxygen Reduction for Lithium-Air Battery Applications, The Journal of Physical Chemistry C 113 (2009) 20127–20134.

[94] C.O. Laoire, S. Mukerjee, K.M. Abraham, E.J. Plichta, M.A. Hendrickson, Influence of Nonaqueous Solvents on the Electrochemistry of Oxygen in the Rechargeable Lithium-Air Battery, The Journal of Physical Chemistry C 114 (2010) 9178–9186.

[95] G.W. Hung, R.H. Dinius, Diffusivity of oxygen in electrolyte solutions, Journal of Chemical & Engineering Data 17 (1972) 449–451.

[96] D. He, C.E. Wong, W. Tang, P. Kovalsky, T.D. Waite, Faradaic Reactions in Water Desalination by Batch-Mode Capacitive Deionization, Environmental Science & Technology Letters 3 (2016) 222–226.

[97] A.S. Yasin, H.O. Mohamed, I.M.A. Mohamed, H.M. Mousa, N.A.M. Barakat, Enhanced desalination performance of capacitive deionization using zirconium oxide nanoparticles-doped graphene oxide as a novel and effective electrode, Separation and Purification Technology 171 (2016) 34–43.

[98] B. Chen, Y. Wang, Z. Chang, X. Wang, M. Li, X. Liu, L. Zhang, Y. Wu, Enhanced capacitive desalination of MnO2 by forming composite with multi-walled carbon nanotubes, RSC Advances 6 (2016) 6730–6736.

[99] A.G. El-Deen, J.-H. Choi, K.A. Khalil, A.A. Almajid, N.A.M. Barakat, A TiO2 nanofiber/activated carbon composite as a novel effective electrode material for capacitive deionization of brackish water, RSC Advances 4 (2014) 64634–64642.

[100] A.G. El-Deen, N.A.M. Barakat, H.Y. Kim, Graphene wrapped MnO2-nanostructures as effective and stable electrode materials for capacitive deionization desalination technology, Desalination 344 (2014) 289–298.

[101] W. Zhang, B. Jia, Toward anti-fouling capacitive deionization by using visible-light reduced TiO_2/graphene nanocomposites, MRS Communications 5 (2015) 613–617.

[102] P.-I. Liu, L.-C. Chung, C.-H. Ho, H. Shao, T.-M. Liang, R.-Y. Horng, M.-C. Chang, C.-C.M. Ma, Effects of activated carbon characteristics on the electrosorption capacity of titanium dioxide/activated carbon composite electrode materials prepared by a microwave-assisted ionothermal synthesis method, Journal of Colloid and Interface Science 446 (2015) 352–358.